Chapter 12
On Line Diagnosis in Induction Motors and Load

Carlos Verucchi and Gerardo Acosta

12.1. Introduction

Induction motors are essential components in the vast majority of industrial processes. The different faults on induction machines may yield drastic consequences for an industrial process. The main problems are related to the increasing costs, and the worsening of the process safety conditions and the final product quality. Many of these faults show themselves gradually. Then the detection of incipient faults allows avoiding unexpected factory stops and saving a great deal of money [1-3]. The kind of faults of these machines is varied. However the most frequent are [4]:

- Opening or shorting of stator phase windings;
- Broken rotor bar or cracked rotor end-rings;
- Static or dynamic air-gap irregularities;
- failures;
- Magnetic wedges.

These faults may be observed through some of the following symptoms [5]:

- Unbalanced air-gap voltages and line currents;
- Increased torque pulsations;
- Decreased average torque;
- Increased losses;
- Excessive heating.

Carlos Verucchi
INTELyMEC (UNCPBA) and CIFICEN (UNCPBA-CICPBA-CONICET), Olavarría, Argentina

It should be noted that some minor faults, which do not endanger the life of a motor, could however lead to a decrease in its efficiency. Given that the efficiency levels of electric motors are constantly monitored and adjusted for the purpose of a worldwide energy consumption reduction [6-8], it is important to recognize incipient faults to avoid inadequate performances.

The reason for such faults may reside in small errors during motor manufacturing, improper use, high level of requirements in motor start-up, ventilation deficiency, and others. Motors actuated by pulse width modulation (PWM) voltage source inverters, have greater probabilities to fail in their bearings [9] and in their stator windings' insulation [10].

Several diagnosis techniques for the identification and discrimination of the enumerated faults have been proposed. Temperature measurements, infrared recognition, radio frequency emissions, noise monitoring or chemical analysis are some of them [5]. References for coils to monitor the motor axial flux may be found in [11], vibration measurement, in [11, 12]. Spectrum analysis of machine line current (called motor current signature analysis or MCSA) is referred to in [13-18], Park's Vector Currents (PVC) Monitoring, in [19, 20], artificial intelligence based techniques are used in [21-23].

The diagnostic possibilities of some of these techniques are not limited only to the motor but also extend to the driven load and to the transmission elements between the motor and the load. In this sense, some of the faults that could be detected and diagnosed would be:

- Misalignment in flexible coupling [25-27];
- Gear box fault [28-32];
- Unbalance mass;
- Cavitation [33], etc.

In these cases, the motor acts as a kind of sensor that monitors the behavior of the mechanical elements of the drive.

The next section will show the evolution degree that the on-line diagnostic techniques have reached for electric drives. Special attention will be given to the analysis of the ability of these techniques for predictive maintenance in industrial applications. To that end, several examples of application in which the authors have experience will be presented.

The section that follows presents the use of an expert system specifically applied to the detection of electrical faults in induction motors based on the measurement of one of the stator currents (MCSA) [15]. Subsequently, the article focuses on a case of misalignment detection in flexible couplings [25]. Finally, we discuss a case of gear teeth wear detection in gear boxes [32].

12.2. Internal Fault Detection in Induction Motors

12.2.1. Motor Current Signature Analysis

From all these approaches proposed in literature, those based on stator current monitoring are advantageous because of its non-invasive feature. One of these techniques is the MCSA, in which rotor faults become apparent by harmonic components around the supply frequency. The amplitude of these lateral bands allows dimensioning the failure degree [5]. Also, the Extended Park's Vector Approach (EPVA), based on the observation of the Park's complex vector module, allows the detection of inter-turn short circuits in the stator winding. This section presents the development of an on-line current monitoring system (CMS) to perform the diagnosis task in a supervisory system [24]. This last task employs both techniques (MCSA and EPVA) in an integrated way, for fault detection and diagnosis in the stator and in the rotor of an induction motor, respectively. The selection of both techniques is due to MCSA as well as EPVA shares the stator current sensing, and then the same information may be used as input for both methods. In this way, current spectral components convey information about the rotor state, while the EPVA is appropriate for the stator windings monitoring, as it will be shown. The proposed CMS uses a National™ data acquisition equipment and is programmed in LabView™. From the acquired current data and the motor features, the CMS estimates the slip and load percentage. Based on experimental observations and on the knowledge of the electrical machine, a knowledge-based system (KBS) was constructed in order to carry out the diagnosis task from these estimated data. The results of each diagnosis are outcomes in the CMS screen in the form of fault modes index. If necessary, a warning is given to put the motor under new observations (i.e., to measure the rotor speed or to change the motor load), or even to verify the power distribution net balance. Experimental results are presented from an induction motor of 380 V, 7.5 HP and 1000 rpm, especially designed for running under different failure circumstances. These results with a high degree of correct diagnosis show a right direction to explore.

When there are broken or even fissured bars, the rotor's impedance exhibits an unbalance. The immediate consequence of such unbalance is the existence of inverse sequence currents. These currents have a frequency that is equal to the product of the slip (*s*) and the supply frequency (*f*). They generate a magnetic field that turns counter motor rotation-wise. This magnetic field is called inverse magnetic field or IMF. The speed of this IMF is given by the expression (12.1):

$$\omega_i^r = -s.\omega_s, \tag{12.1}$$

where ω_{ri} is the speed of IMF, s is the slip and ω_s is the angular supply frequency.

If translated to stationary co-ordinates, such a speed may be re-written as:

$$\omega_i^s = -s.\omega_s + \omega_r = (1-2.s).\omega_s, \tag{12.2}$$

where ω_r is the rotor speed.

The amplitude of IMF depends on two features. The first is the unbalance degree in the rotor circuit (number of broken bars), and the second is the value of the current in the rotor bars. This last depends on the motor's load state. In this way, the IMF originated in the rotor's impedance unbalance produce harmonic currents of frequency *(1-2.s).f* in the stator windings. These currents interact with the main magnetic field and set a torque over the rotor, which oscillates with a frequency of *2.s.f* [18]. This pulsating torque provokes an oscillation also in the rotor speed. The amplitude of this oscillation is a function of motor's load inertia. As a reaction of such speed perturbation, new currents arise in the stator at a frequency *(1±2.s).f*. The new current component at frequency *(1-2.s).f* is superimposed with the original, and then modifies its amplitude. In this way, it is concluded that rotor faults in an induction motor, can be determined from the observation of the sidebands in the stator current spectrum, in the neighbourhood of both frequencies given by equation (12.3).

$$f_{SB} = (1 \pm 2.s).f, \tag{12.3}$$

An example of the current spectrum of a motor with this fault is shown in Fig. 12.1.

Fig. 12.1. Frequency spectrum of one phase stator current of a motor with three broken bars and full load.

As regards as the amplitude of these stator current sidebands, they depend on three factors: the motor load inertia, the motor load torque, and the severity of the fault. So, the first two factors must be suppressed in order to analyse, as independently as possible, the one of concern for the present application.

The motor load inertia can be avoided if the sum of both sidebands component is considered, as proposed in [16]. As regards as the motor load torque, there is always a relationship between the amplitude of the sidebands and the amplitude of the fundamental component of the stator current at the supply frequency. Then, working with normalised amplitude values as regards as this supply frequency component, allows to partially avoid the influence of this second factor. However, sidebands reveal faults more clearly with high values of slip. Then it is recommended that the diagnosis were done with the motor running near its nominal load.

Then, a severity factor can be defined as:

$$S_{RF} = \frac{I_{(1\pm 2.s)f}}{I_1}.100, \tag{12.4}$$

where SRF is the severity rotor fault, $I_{(1\pm 2.s).f}$ is the sum of amplitude of sidebands, and I_1 is the amplitude of the fundamental component of the stator current.

12.2.2. Extended Park's Vector Approach

The Park's transform [34], allows representing the variables of a three phases machine through a co-ordinates system with two perpendicular axes. The components of the stator currents in the direct and quadrature axes (D y Q) are computed by means of the following expressions:

$$i_D = \sqrt{\frac{2}{3}}.i_A - \sqrt{\frac{1}{6}}.i_B - \sqrt{\frac{1}{6}}.i_C, \tag{12.5}$$

$$i_Q = \sqrt{\frac{1}{2}}.i_B - \sqrt{\frac{1}{2}}.i_C, \tag{12.6}$$

where i_A, i_B and i_C are the stator currents. Under ideal conditions, that is, when a normal behaviour motor is fed with a sinusoidal, balanced and positive sequence three-phases current system, the Park's components or Park's Currents Vector (PVC) results in:

$$i_D = \frac{\sqrt{6}}{2}.I_{\max}.\sin(\omega_s.t), \tag{12.7}$$

$$i_Q = \frac{\sqrt{6}}{2}.I_{\max}.\sin(\omega_s.t - \pi/2). \tag{12.8}$$

In this expression I_{max} is the maximum stator current value and t is the time variable. Equations (12.7) and (12.8) describe a perfect circle centered in the origin of the plane D-Q, with constant radius equal to ($\sqrt{6}/2$). Fig. 12.2 presents the PCV from a Lab experiment of an induction motor under normal conditions. The small variations in the vector radius are due to small unbalanced voltages of distribution system. In the same way, the space and slot harmonics introduce small perturbation in the vector radius. They are negligible for the present analysis and then are filtered in the data acquisition stage.

One of the most usual faults in induction motors consists of inter-turn short circuits. In this case, the motor behaves like an unbalanced load, and the stator currents are no longer a balanced system. This abnormal behaviour causes an oscillation in PVC radius, turning the original circle into elliptical shapes, as may be seen in Fig. 12.3 for a motor with two coils of phase a (over a total of sixteen) in short circuit. The inclination of the ellipse mayor axe shows the phase in which the fault was produced [20].

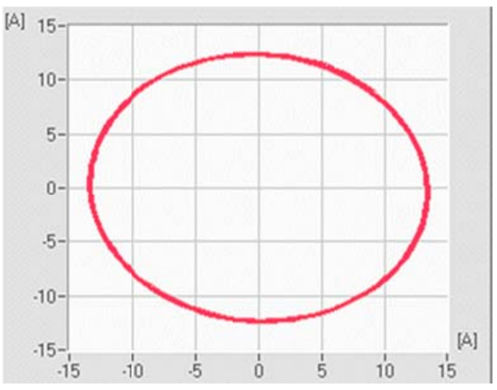

Fig. 12.2. Geometric locus for the Park's Currents Vector for a motor with normal behaviour.

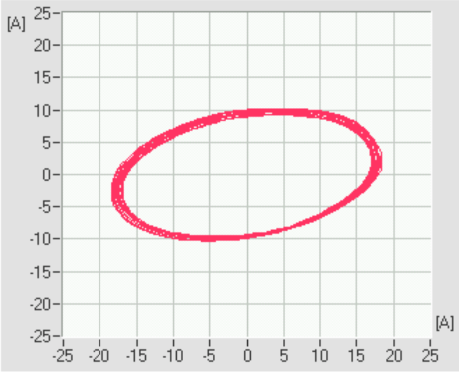

Fig. 12.3. Geometric locus for the Park's Currents Vector for a motor with coils in shortcut.

S. Cruz and A. Marquez Cardoso [19] propose to observe the radius of the geometric locus of the PVC along time in order to obtain a fault diagnosis. Effectively, as this radius oscillates between a maximum and a minimum twice in a supply frequency cycle, it may be decomposed in a Fourier's series. This series presents a direct current component plus a component in twice the net frequency (I_{2NF}). This is shown in Fig. 12.4 in which it is depicted a motor with stator coil faults. The amplitude of I_{2NF} is again related to the dimension of the fault and then a new severity factor may be defined as [19]:

$$S_{SF} = \frac{I_{2NF}}{I_{cc}}.100. \tag{12.9}$$

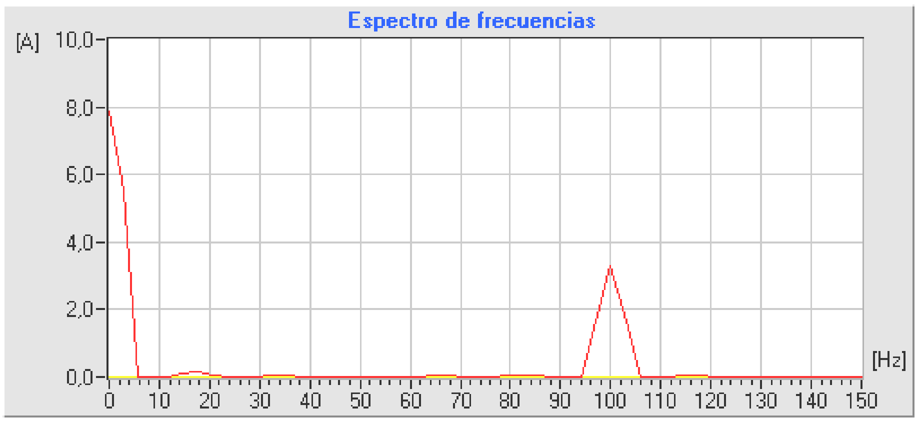

Fig. 12.4. Harmonic analysis of the Park's Vector module.

It is important to take into account that this severity factor varies with motor load, decreasing as the motor approximates to its nominal load.

12.2.3. Towards an Integrated Fault Diagnostic System

One aim of the present work was to combine the previous techniques and, in some way, to take the better of them in a single, integrated diagnostic system.

From the stator spectral analysis (MCSA) it is possible to detect rotor as well as stator winding faults, as presented in [35]. However, in this last case, the frequency characterising the fault must be computed considering the motor poles number, the slip, and the winding features. Also, another handicap of this approach is that it is not possible to relate the fault severity with the amplitude of these frequencies characterising the fault. In contrast, in EPVA the frequency to discriminate a fault is always fixed and twice the supply frequency. Also EPVA only uses the current fundamental component to draw the Park's geometric locus. It is then possible to filter any higher frequency making the procedure more robust in front of noise and perturbations. This is the reason for selecting this last approach for fault detection and diagnosis in the stator.

To obtain a useful diagnosis for the rotor of the induction motor, some authors describe the viability of detecting broken bars by means of the PVC [36]. It is not clear yet that one method is better than the other for this case. However, as the MCSA has been used for so long, giving enough proofs of utility at industrial environments [35], it is the approach selected in this work for detecting and diagnosing rotor electrical faults.

In a normal running, the CMS set the state of the rotor and then the state of the stator winding. It is necessary to determine the frequencies at which harmonic components will appear, because a torque that oscillates may be confused with a fault mode [36]. In order to achieve this, a motor slip is estimated from the no-load current, assuming it is in quadrature with the load component. With both currents a phasorial diagram may be built (as shown in Fig. 12.5). From the measured stator current (I_S) in Fig. 12.5, the load component is computed for the present running state. This value is compared to the load component of the nominal current to obtain a motor load index (*MLI*). Then from *MLI* and the nominal speed, the motor slip is estimated (S_E), according to the scheme of Fig. 12.6. From S_E and equation (12.3), frequencies are computed and the fault components may be searched around them, as it is shown in Fig. 12.7. In order to avoid detecting peaks due to perturbations, components must be symmetrically placed from the fundamental frequency, and with similar modules.

Once these preliminary computations are done, a severity factor for the rotor (S_{RF}) is computed from expression (12.4). Then to obtain a final diagnosis, the CMS resorts to some expertise coded in a production system format, that is, a rule-base. As it may be seen, the diagnostic system is symptom driven and uses abduction to give an outcome [37]. In consequence, the working hypotheses for a successful diagnosis, is to consider a closed cause-symptoms universe, with every fault mode known beforehand. This strong assumption may be easily surpassed taking into account the unknown fault as a possible fault mode. Faults are then classified in “light”, “moderate” and “strong”. It was observed for the SSF that normal induction motors have a value within 3 %. Naturally, as the fault severity increases, the factor must also increase. Effectively, the fault discrimination in light, moderate and severe was done based on the short circuit turn percentage in one phase. In order to be considered as a light fault, it shall allow the motor to keep on running without the need of an immediate stop. A moderate fault is the one producing overloads in the remaining phases, such that they push the motor to run in a risky mode. A severe fault also produces current overload in the other phases, but in such a level that it causes risky mechanical vibrations. The thresholds separating one kind of fault from another were determined from experimental observations.

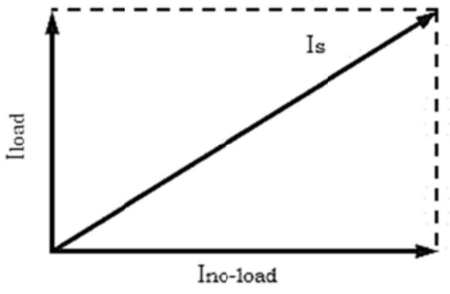

Fig. 12.5. Load percentage estimation.

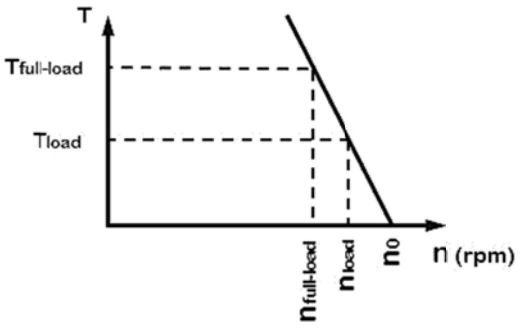

Fig. 12.6. Slip’s estimation.

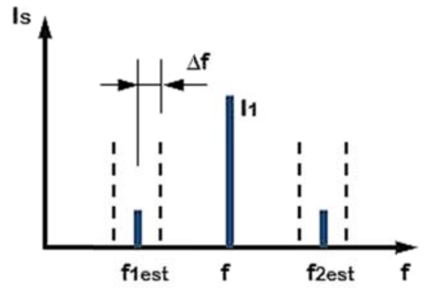

Fig. 12.7. Identification of the components of harmonic currents.

In a normal running, the developed CMS may also give some warnings to improve the diagnosis, such as a repetition of the test with a higher/lower load level. As an example, one of these rules is presented next:

If S_{SF}*>=6.5 % AND* S_{SF} *< 8 % AND Load Factor >= 0.5*

then

Fault: one coil in short circuit (Moderate)

Warning: repeat diagnostic procedure with half the load for a better diagnosis.

As regards as the stator faults, the CMS computes the geometric locus of the PCV. Then its radius is decomposed in a Fourier series and a measure is done over the component with twice the supply frequency, as explained in Section 12.2.2. The severity factor (S_{SF}) is obtained from equation (12.9). Again, the knowledge base classifies the fault and may give hints to improve results.

12.2.4. Experimental Results

12.2.4.1. The Experimental Prototype

The CMS proposed in this work consists of a data acquisition system sampling the stator currents from current transformers. The test bank is an induction motor dragging a direct current generator with variable load. The acquisition and human-machine interface tasks were developed with LabView. In Fig. 12.8 there is a schematic diagram, and in Fig. 12.9, a snapshot of the experimental prototype used in this research.

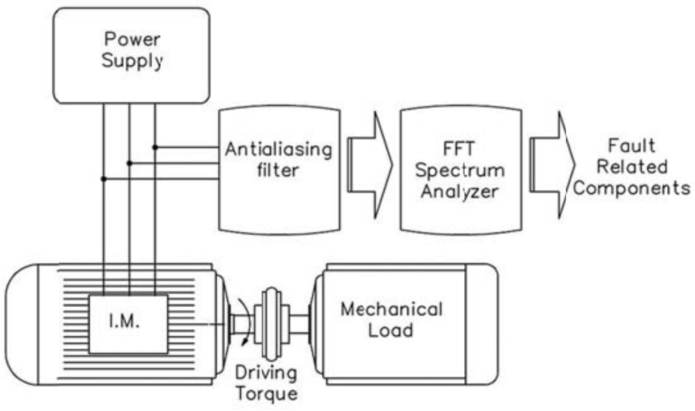

Fig. 12.8. A diagram of the experimental prototype.

Fig. 12.9. A snapshot of the experimental prototype.

The motor under diagnosis for these tests consists of an induction motor of 6 poles and 50 [Hz] that allows changing rotors with different number of broken bars and with access to diverse points of the stator winding.

12.2.4.2. Case Study 1

Two broken bars in rotor and normal stator. The CMS estimates a 65 [%] motor load, the motor speed yielded 989 [rpm], and the slip was of 0.011. As a consequence of this, the frequencies to look for rotor faults were 48.9 [rpm] and 51.1 [rpm], using equation (12.3). Then the system searches for maximum in a range near these frequencies, verifying they are approximately at the same distance from the fundamental component. Components of –140.9 [dB]@49.0 [Hz] and of –119.4 [dB]@50.9 [Hz], were found. As the load factor is between 50 and 75 [%], and the amplitude of these components was in the range of –100 a –150 [dB], the rule base states that “There is a moderate fault in rotor” and gave a warning “repeat diagnostic procedure with a higher load for a better diagnosis”. Also the CMS computed the stator current components among D and Q axes and obtained the frequency spectrum of Park’s vector. It rises an average component of 5.93 [A] and a component of 0.12 [A]@100 [Hz]. With these data, the SSF using equation (12.9) results of 2.02 [%]. As this is smaller than the tolerance threshold of 3 [%], the CMS gave and outcome of “No faults observed in the stator”.

12.2.4.3. Case Study 2

Three broken bars in rotor and normal stator. The CMS acquisition performance may be seen in Fig. 12.10. The load factor was estimated in 0.93 [%] and the frequencies to look for faults were set using equation (12.1). As the motor is near its nominal load the outcome for this case was “There is a strong fault in rotor”. In Fig 12.10 harmonic components due to faults were highlighted using a logarithmic scale. The CMS also states that “No faults observed in the stator”. In effect, for the stator, the SSF is less than the 3 %, which is considered as normal.

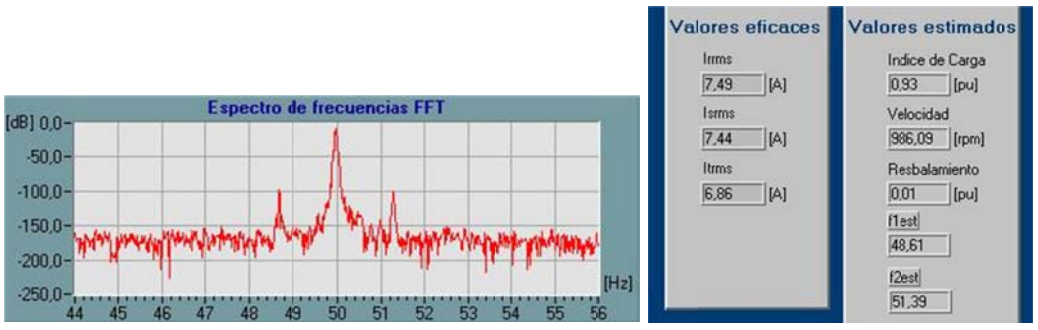

Irrms 7,49 [A]
Isrms 7,44 [A]
Itrms 6,86 [A]
Indice de Carga 0,93 [pu]
Velocidad 986,09 [rpm]
Resbalamiento 0,01 [pu]
f1est 48,61
f2est 51,39

Fig. 12.10. Results from CMS for case study 2.

12.2.4.4. Case Study 3

Normal rotor and short circuit in 12 [%] of stator coils in one phase. The CMS’s human-machine interface, consisting of the Park’s Current Vector depicted and its decomposition in Fourier’s series with diagnostic information, is showed in Fig. 12.11. The SSF was 3.2 [%] with the induction motor running without load and the knowledge base inference was “There is a light fault in stator”. The CMS also reported “No faults observed in the rotor”. In this last case, the SSR could not be computed because the amplitude of stator current sidebands is small enough to be confused with the ripple in the acquired signal.

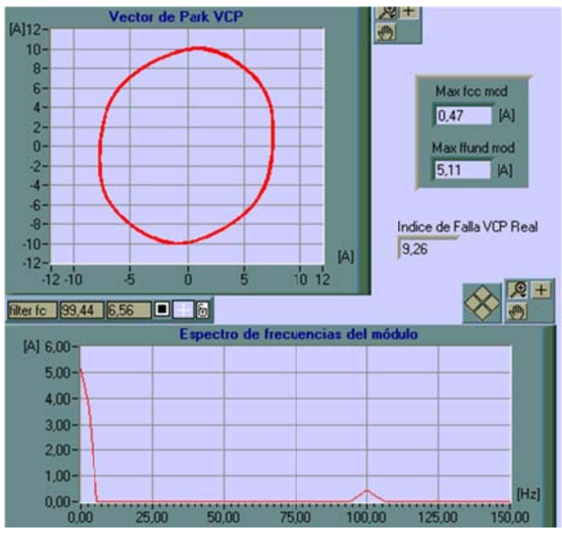

Max fcc mod 0,47 [A]

Max Ifund mod 5,11 [A]

Indice de Falla VCP Real 9,26

filter fc 99,44 6,56

Fig. 12.11. Results from CMS for case study 3.

12.2.4.5. General Comments

It is important to take into account that the computed fault indexes may have a value different to zero even with new and without fault motors, as explained in Section 12.3. This is due to the motor may have little abnormalities in construction (obviously depending on its quality control), and also because of unbalanced supply network, internal errors in sensors, quantification error, and others. Then, in order to avoid false positives when diagnosing, a special attention must be given to detection threshold determination. The performance of the whole system will depend on threshold selection and tuning.

Beyond the presented case studies, several laboratory tests were done over the CMS with this experimental prototype, and obtained results are shown in the following Table 12.1. These tests were done with different kind of faults, different degrees of severity and with the motor in different operating points.

Another important hint to remark, from these laboratory tests, is that while the SSF factor reflects the supply network unbalances, the SRF factor, does not.

Table 12.1. Laboratory tests of CMS with the prototype of Fig. 12.9.

Number of cases	**Correct Diagnosis**	**Incorrect Diagnosis**	**Unknown Diagnosis**
25	21	3	1

Based on the several techniques for fault detection and diagnosis of induction machines proposed in literature, the ones considered most promising were selected. The selection criteria were: non-invasive technique, minimum number of measured variables, discrimination power, and prior motor information to yield a diagnosis.

The obtained CMS gives general conclusions about the motor state, in a user friendly interface. It was easily developed in Lab with commercial products. The added feature of a knowledge base confers the possibility of considering sensors fault or even unbalances in the supply network, as well as a qualitative classification of faults in light, moderate and strong. In those cases of insufficient motor load, the system is able to recommend a warning for a better measure.

12.3. Mechanical Faults Detection Beyond the Motor

12.3.1. General Comments

Progress in the implementation of non-invasive techniques has made possible to extend the diagnosis of faults to the kinematic chain between the motor and load, even to the load. In these cases, it is often necessary to monitor other electrical variables of the motor, such as the electric torque or the active power consumed [25]. To do this, it is necessary to measure not only the stator currents but also the voltages connected to the motor. In [28-30], different techniques for fault detection in gear box driven by induction motors are proposed. In such cases, it is possible to detect gear-teeth wear or breakage from the analysis of the frequency spectrum of the stator currents or the estimated electric torque.

Regarding the driven load, literature presents background on the detection of anomalies from the analysis of electrical variables. For instance, the detection of anomalies in the table of a coal mill is presented in [30]; in [35], the detection of anomalies in an air compressor from the motor variables is shown, and, the detection of cavitation in hydraulic systems with identical strategy is studied in [33].

A study based on the tracking of the stator current and of the active power consumed by the motor to detect misalignment between the motor axes and load is presented in [26]. This paper presents a model that determines the frequencies associated with fault and through experimental tests the feasibility of the proposed method is demonstrated. These tests however are limited to elastic couplings (Rubber Tire-type Couplings) and misalignment on the coupling system may be of great consideration. Results show for example angular misalignment of about 1 to 3 degrees. Though these misalignment angles are within admissible values for elastic couplings, it is important to highlight the capability of the technique for detecting minor misalignments, as they can raise the level of vibration to dangerous levels. A comparison between the MCSA and the vibration analysis can be observed in [27]. This comparison demonstrates that the ability to detect misalignment of MCSA and traditional techniques based on vibration analysis is similar. In addition, [38] also proposes an algorithm able to diagnose faults due to misalignment and mass imbalance for different load conditions. This algorithm compares the fault frequencies of the stator currents with a predetermined admissible value. However, this comparison does not provide criteria to determine failure thresholds. It does not establish differences between different types of couplings either.

This work focuses on misalignment detection. Unlike other works related to the subject, it includes the coupling parameters as variables. In fact, given that there are different choices for power transmission, their comparison is carried out to show the proposed detection technique effectiveness for the most common couplings. Then, it becomes important to establish the criteria to relate the most commonly used fault indicators and angular and radial misalignments.

The theoretical bases that allow deducing how misalignment events occur on the electric motor torque and the stator current are also presented. Then, experimental results are presented for different types of couplings, and finally conclusions are drawn.

12.3.2. Misaligned Drives Model

It is important to distinguish two types of potential misalignment: angular misalignment and radial misalignment. Angular misalignment occurs when there is an angular deviation between the motor shaft and load. This situation is illustrated in Fig. 12.12a. The degree of misalignment is represented by angle α between the two shafts. When the shafts are perfectly parallel to each other, but not on the same line, radial misalignment occurs. This situation can be observed in Fig. 12.12b. Radial misalignment is more severe as the distance between the two axes of rotation becomes greater. Such distance is indicated as d in Fig. 12.12b and it will be taken as a reference value to indicate degrees of radial misalignment in experimental tests.

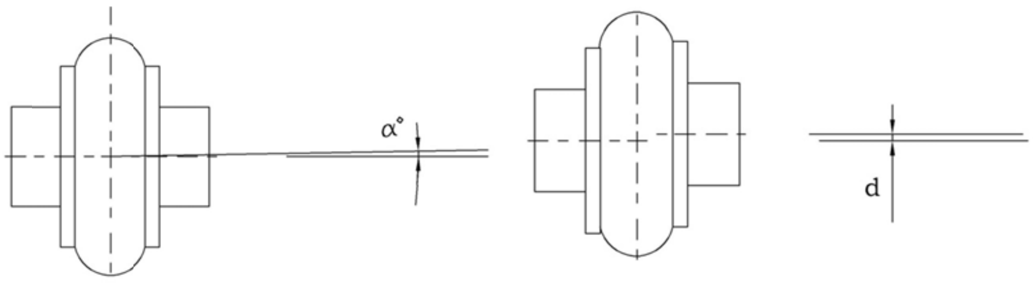

(a) (b)

Fig. 12.12. Angular Misalignment (a), and Radial Misalignment (b).

Misalignment situations are very common in industrial applications. They usually arise during the assembly process and can be associated to the motor fasteners, the gear box or other drive components. They can be also due to the preloads produced in pipes or any other components associated with the load. Misalignment can not only occur as the two types described in Fig. 12.12 but also as a combination of them.

Mostly elastic couplings are used in these applications. These couplings allow dampening sudden load torque disturbances, avoiding knocks on the wheels of the gear boxes, and reducing vibrations during load transmission. All elastic couplings are able to bear small levels of misalignment. The main purpose of the flexible couplings is to allow misalignment due to the assembly of connected rotors and due to the changes of temperature and operation. In addition, the flexible couplings separate mechanically the rotors so that the rotodynamic design of individual rotors can be carried out separately. However, misalignments of any degree reduce couplings lifetime, increase losses [15], and generate mechanical vibrations and bending stress on axes, which may affect the bearing system severely.

Fig. 12.13 shows the four different elastic couplings evaluated in this work, mostly used in industrial applications [39]. Jaw Couplings (Fig. 12.13a) are an inexpensive and easy to mount option for standard power applications. They are able to dampen moderate-impact low-vibration loads. Couplings of this type are not torsionally rigid and can bear some degree of radial and angular misalignment as well as axial movement on the shaft. Gear Couplings (Fig. 12.13b), on the other hand, show torque high density and are torsionally rigid. They can be either flexible or flexible-rigid couplings. Flexible couplings are able to bear radial and angular misalignment. Metal Ribbon Couplings (Fig. 12.13c) allow torsion as well as angular and radial misalignment. They require lubrication and have certain limitations of temperature and speed. Finally, Rubber-type Couplings, (Fig. 12.13d), are able to bear some degree of misalignment at all levels without imposing excessing loads on the bearing system. Their damping properties allow reducing torsion vibrations and oscillations.

As it is shown in [26], misalignment modifies the motor torque according to the following equation:

$$T_k = \left[\frac{1}{\cos\alpha} - \frac{\sin^2\alpha}{2\cos\alpha} - \left(\frac{\sin^2\alpha}{2\cos\alpha} \cos 2\theta_l \right) \right] T_l, \tag{12.10}$$

where α is the misalignment angle (Fig. 12.12a), θ_l is the angular position of the load with regards to its own rotation axis and T_l is the load torque. Equation (12.10) shows that, when α takes a value other than 0, the level of torque the motor must overcome increases progressively its mean value and also incorporates a frequency component $2.\theta_l$. This component amplitude increases with misalignment. As for the motor stator current, misalignment occurs through the sidebands around the fundamental component at the frequencies given by:

$$f_s = f \pm n f_r, \tag{12.11}$$

where f_r is the rotational frequency and n are integers greater than 0. Thus, the fault under study will become evident both on the electrical torque as on the stator current.

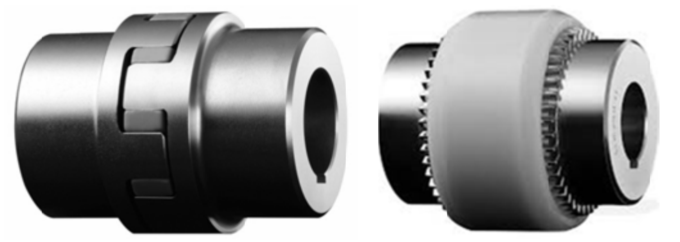

(a) Jaw Coupling (b) Gear Coupling

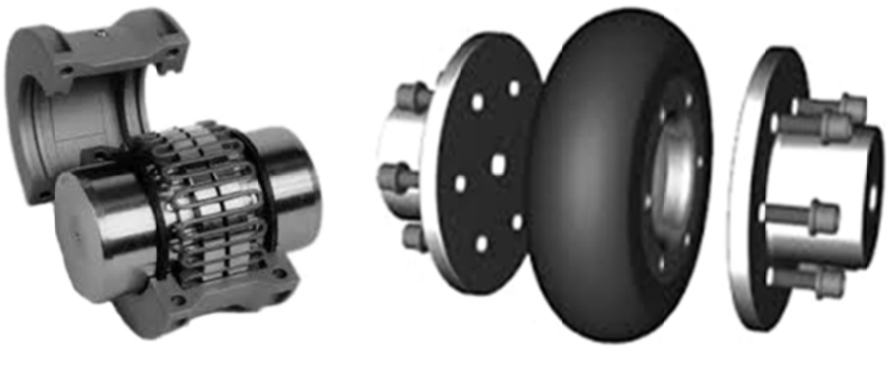

(c) Metal Ribbon Coupling (d) Rubber Tire-type Coupling

Fig. 12.13. Different Types of Couplings.

This model has been obtained considering a universal coupling between the motor and load, and therefore does not take into account the characteristics due to the coupling nature. Thus, it only provides information about the frequencies associated with failure in both the torque and the stator current.

12.3.3. Fault Detection Method

Two of the most used non-invasive techniques for fault detection in electrical drives are MCSA and LTSA [40]. These techniques consist in analyzing the frequency spectrum of the stator current and torque. Monitoring of the amplitude of the frequency components given by equations (12.10) and (12.11) allows monitoring the alignment status of a particular coupling.

Generally, it is not possible to measure directly the torque provided by the motor and therefore, a rough estimation of it is used. Such estimation is carried out from the measurement of the stator voltages and currents according to the following equation [41]:

$$T_e = (3/2)(P/2)(\lambda_{ds}.i_{qs} - \lambda_{qs}.i_{ds}), \tag{12.12}$$

where P is the number of poles, and λ and i are flux and current on axes d and q. Flux linkagesare obtained as,

$$T_e = (3/2)(P/2)(\lambda_{ds}.i_{qs} - \lambda_{qs}.i_{ds}), \tag{12.13}$$

where voltages and currents are denoted as follows:

$$\mathbf{v}_s(t) = v_{qs}(t) + \mathrm{j}\ v_{ds}(t), \tag{12.14}$$

$$\mathrm{i}_s(t) = i_{qs}(t) + \mathrm{j}\ i_{ds}(t), \tag{12.15}$$

Torque estimation requires besides sensing currents and voltages, knowing the stator resistance and number of poles of the motor.

The structures of the LTSA and MCSA methods are presented in a block diagram in Fig. 12.14.

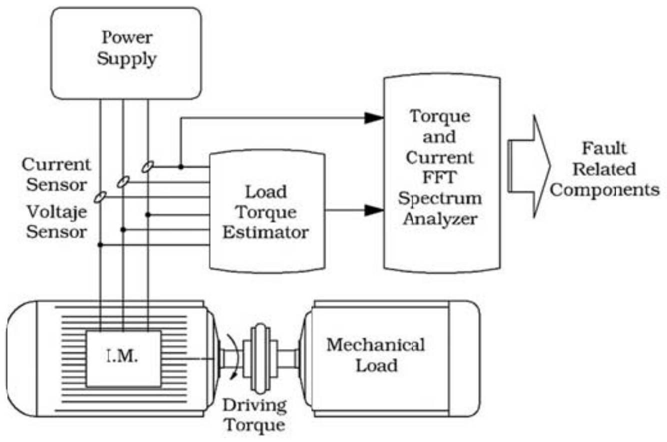

Fig. 12.14. Functional Block Diagram of the LTSA and MCSA Fault Detection Methods.

12.3.4. Experimental Results

Some experimental tests are designed to determine the capability to detect misalignment of the proposed techniques when applied on different couplings. For this purpose, a 3 kW, 4 pole, 50 Hz 380 V induction motor, coupled to a DC machine is used. The motor is mounted on a swivel base that allows imposing angular misalignment conditions to the coupling. Radial misalignment is controlled by the horizontal displacement of the motor respect to load. This assembly can be observed in Fig. 12.15. All the couplings used in these tests were selected depending on the transmitted torque, rotation speed, load and the rotor shaft diameters, as required by commercial catalogs. Data were collected from a 16 bit National Instruments Acquisition Card and LabView^{TM} software at a rate of 10 k samples per second.

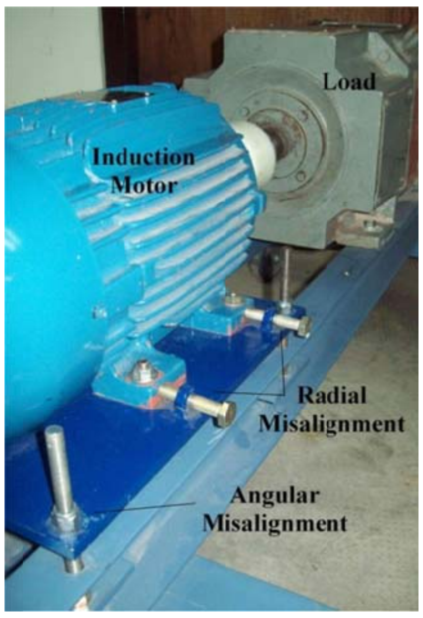

Fig. 12.15. Laboratory Assembly.

First, a comparison of the diagnosis variables is carried out for alignment and a 1.5 mm radial misalignment. For this comparison, a Jaw Coupling is used. Fig. 12.16 shows the frequency spectrum of the estimated torque for the case of shaft alignment. These results correspond to 75 % of the nominal power. For such load condition, the rotational speed of the motor is 1452 rpm and the rotational frequency is 24.2 Hz is. An additional component of the rotational frequency, (f_r), is also observed in Fig. 12.16. This component may be due to either load mass imbalance or rotor eccentricity. The same figure also shows the absence of components at twice the rotation frequency ($2f_r$), which, as it is shown in Section 12.2, are able to detect fault misalignment. Fig. 12.17 shows the frequency spectrum for 1.5 mm radial misalignment. In this particular case, it can be clearly observed a component ($2f_r$), and another component, ($3f_r$) of greater amplitude. These components clearly show misalignment between the motor axis and load. Furthermore, it can be observed that the component f_r for misalignment is higher than that for aligned shafts. This increase can be explained by the additional forces due to misalignment on motor shaft extension. Such forces increase the rotor eccentricity which appears a component at f_r. From this comparison, it can be concluded that as for component $2f_r$ as for $3f_r$, they both allow diagnosing faults due to misalignment.

Regarding currents, the fault under study appears at the sidebands shown in equation (12.11). Figs. 12.18 and 12.19 show the frequency spectrum of the stator current for the alignment and load conditions shown in Fig. 12.16 and Fig. 12.17. Fig. 12.18 shows the sidebands at frequencies $f \pm f_r$, associated to the component f_r, which appear in the motor torque (Fig. 12.16), whereas it cannot be observed components at $f \pm 2f_r$ or $f \pm 3f_r$. Fig. 12.19 shows misalignment in the coupling expressed by means of components at $f + 2f_r$ and $f + 3f_r$.

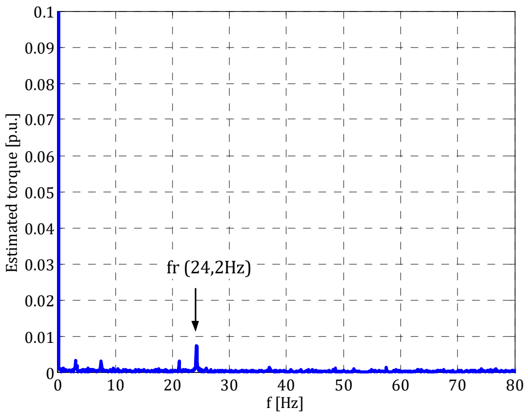

Fig. 12.16. Estimated Torque Frequency Spectrum, Jaw Coupling, 75 % of load, aligned Shafts.

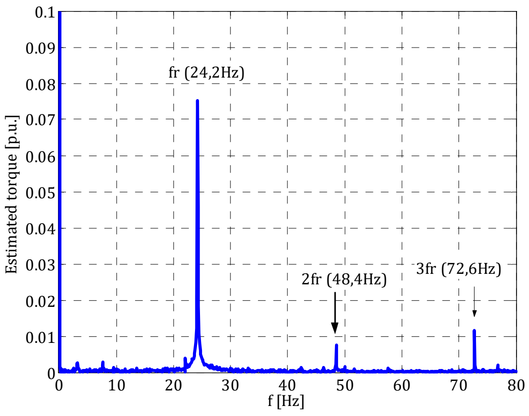

Fig. 12.17. Estimated Torque Frequency Spectrum, Jaw Coupling, 75 % of Load, 1.5 mm, Radial Misalignment.

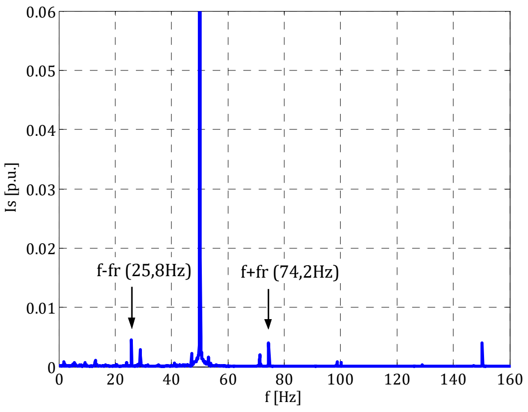

Fig. 12.18. Stator Current Frequency Spectrum, Jaw Coupling, 75 % of Load, Aligned Shafts.

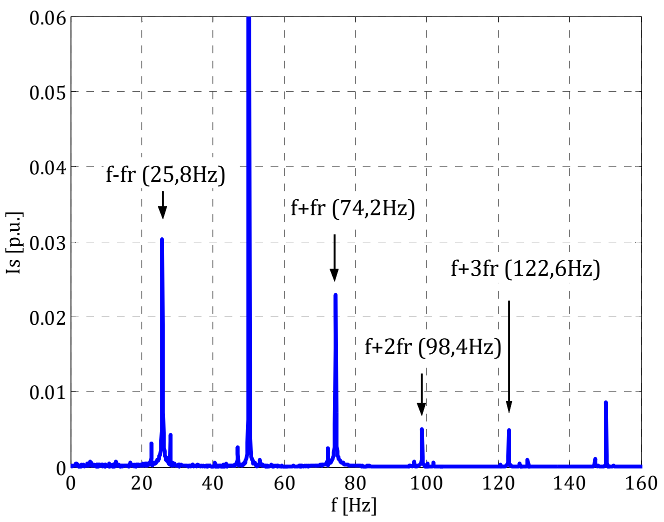

Fig. 12.19. Stator Current Frequency Spectrum, Jaw Coupling, 75 % of Load, 1.5 mm Radial Misalignment.

Then, from this first study, it is possible to check both the analysis of the stator currents and the torque estimation to demonstrate radial misalignment. Similar tests allow to extend these conclusions to angular misalignment cases.

Results from Figs. 12.16 to 12.19 are obtained with 75 % of the nominal load. However, as it can be observed in [38], the amplitude of the components associated to the fault under analysis may vary significantly with the motor load. With the objective of evaluating the motor behavior for different load levels, several tests were carried out for different degrees of misalignment and for variable load values ranged between 25 and 100 % of the nominal power. All the tests were performed with different coupling, starting with the same alignment condition and then varying radial and angular misalignment. The remaining variables for the experiments were kept unchanged. Figs. 12.20 and 12.21 show the amplitude of the component at *2fr*, expressed in Nm and p.u., respect to the mean torque, respectively. These figures allow comparing the obtained components for alignment and for two different levels of radial misalignment, both in a Jaw Coupling. It can be deduced from the curves in the same figures that the fault indicators, expressed in both Nm. and p.u., show a tendency to decrease as the motor load increases. Moreover, it can be clearly observed that this relationship between indicators and load is nonlinear. Also, these fault indicators increase with the fault severity (0.75 mm and 1.5 mm misalignments, respectively).

Figs. 12.22 and 12.23 show the results for radial misalignment at the component at $3f_r$. Conclusions are similar to those for the component at $2f_r$. The values of the component at $3f_r$ show a strong dependence on load, to such an extent that for certain load levels, the most severe fault appears less noticeable than the least one. This observation allows concluding that the indicator that best suits misalignment is the component at $2f_r$.

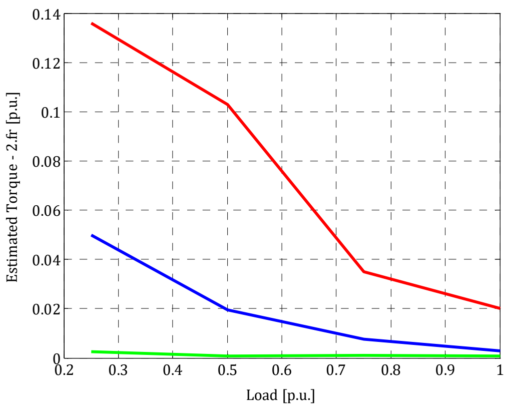

Fig. 12.20. Components at twice the rotation frequency. Values in p.u. Green: Alignment, Blue: 0.75 mm Radial Misalignment, Red: 1.5 mm. Radial Misalignment.

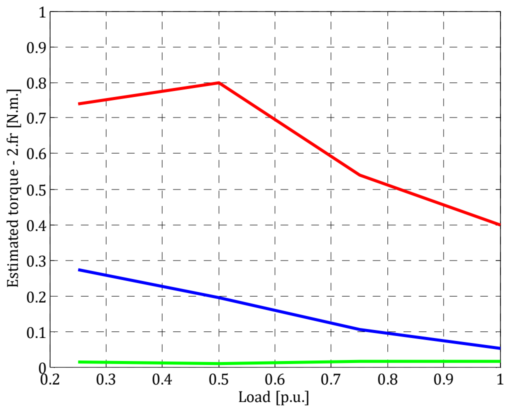

Fig. 12.21. Components at twice the rotation frequency. Values in N.m. Green: Alignment, Blue: 0.75 mm Radial Misalignment, Red: 1.5 mm. Radial Misalignment.

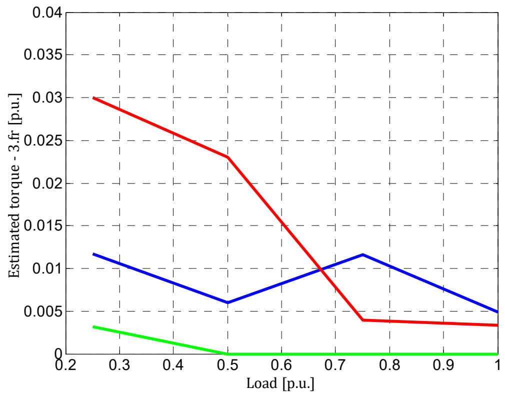

Fig. 12.22. Components at three times the rotation frequency. Values in p.u. Green: Alignment, Blue: 0.75 mm Radial Misalignment, Red: 1.5 mm Radial Misalignment.

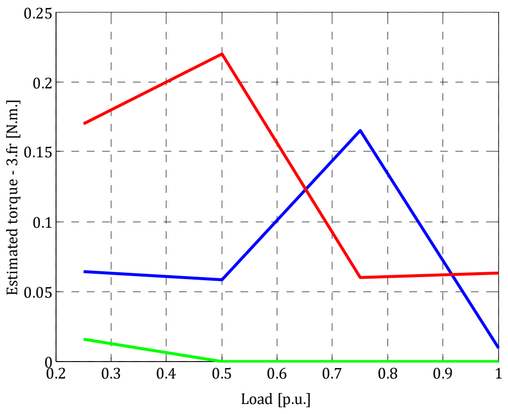

Fig. 12.23. Components at three times the rotation frequency. Values in N.m. Green: Alignment, Blue: 0.75 mm Radial Misalignment, Red: 1.5 mm Radial Misalignment.

Figs. 12.24 and 12.25 present results for angular misalignment. Misalignment levels are ranged from 0.5° to 1°. The Jaw Coupling used for this test is the same used in previous tests. Conclusions are similar to those obtained for radial misalignment, i.e., a decrease in the fault indicator, in p.u. and Nm, with a decrease in load and erratic variation of the component $3f_r$.

It is important to notice that the misalignment levels used for the comparison, as for radial as for angular misalignment, are low as the couplings under study are also able to bear high misalignment degrees.

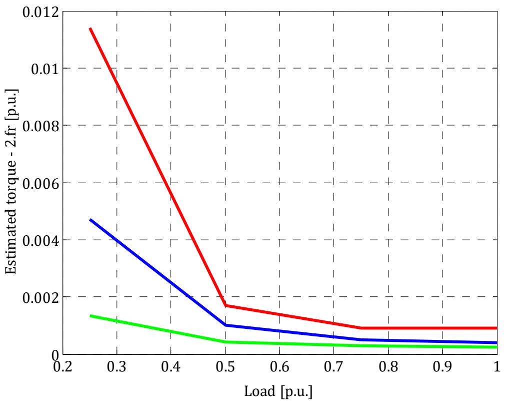

Fig. 12.24. Components at twice the rotation frequency. Values in p.u. Jaw Coupling. Green: Alignment, Blue: 0.5° Angular Misalignment, Red: 1° Angular Misalignment.

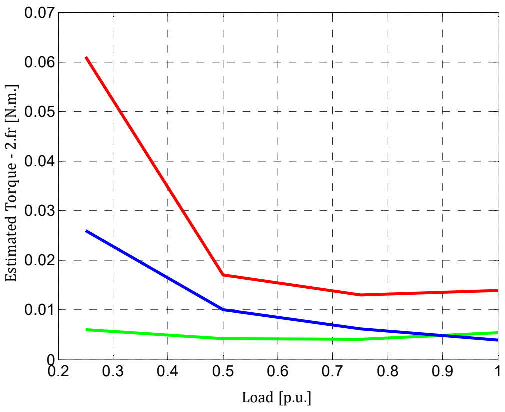

Fig. 12.25. Components at twice the rotation frequency. Values in N.m. Green: Alignment, Blue: 0.5° Angular Misalignment, Red: 1°Angular Misalignment.

The results obtained using a Jaw Coupling presented in Figs. 12.20 to 12.25 allow validating the conclusions drawn in [26, 38]. The only difference is that it considers lower levels of misalignment to demonstrate the capability to detect incipient faults. The same experiments carried out using the Jaw Coupling are repeated but using the other couplings shown in Fig. 12.13. Tables 12.2 and 12.3 display the values of the estimated torque components for 1° angular misalignment (Table 12.2) and 1.5 mm radial misalignment (Table 12.3), for each four couplings under study.

Similarly, Tables 12.4 and 12.5, present the results obtained for the stator currents (MCSA). In this case, the values presented in the tables correspond to the RMS obtained from both sidebands components.

Table 12.2. Torque at *2fr* for 1°angular misalignment. Values expressed in % of the mean T.

Load (%)	**Rubber Tire-type Coupling**	**Jaw Coupling**	**Gear Coupling**	**Metal Ribbon Coupling**
25	0.22	1.13	0.67	0.51
50	0.16	0.17	0.55	0.15
75	0.09	0.14	0.45	0.09
100	0.05	0.07	0.29	0.07

Table 12.3. Torque at *2fr* for 1.5 mm radial misalignment. Values expressed in % of the mean T.

Load (%)	Rubber Tire-type Coupling	Jaw Coupling	Gear Coupling	Metal Ribbon Coupling
25	0.24	13	2.6	4.1
50	0.14	10	3.7	2.8
75	0.06	4.1	0.66	2.7
100	0.07	2.1	0.13	1.6

Table 12.4. Stator current (RMS) for 1°angular misalignment – Values expressed in % of the fundamental component.

Load (%)	Rubber Tire-type Coupling	Jaw Coupling	Gear Coupling	Metal Ribbon Coupling
25	0.14	0.15	0.31	0.18
50	0.09	0.11	0.34	0.11
75	0.06	0.09	0.30	0.06
100	0.04	0.06	0.25	0.05

Table 12.5. Stator current (RMS) for 1.5 mm radial misalignment – Values expressed in % of the fundamental component.

Load (%)	Rubber Tire-type Coupling	Jaw Coupling	Gear Coupling	Metal Ribbon Coupling
25	0.14	5.7	1.1	2.7
50	0.07	7.3	2.9	1.5
75	0.05	3	0.48	2.2
100	0.04	2	0.13	1.9

The results obtained using the Jaw Coupling and the other couplings show similar tendency. That is, they show a decrease in the indicators as the motor load increases. In addition, it becomes clear that the obtained values, as for the estimated torque as for the stator current, are significantly different for the different couplings. In fact, for identical misalignment and load conditions, the results obtained for the different couplings show variations as for angular as for radial misalignment.

Figs. 12.26 and 12.27 show the results for the estimated torque and stator current for angular misalignment. Regarding both variables, it can be observed an important difference between the indicators associated to the Gear Coupling and those of the other couplings. The Gear Coupling shows a really low tolerance to angular misalignment due to the torque high-harmonic components of these couplings. As for the rest of the couplings under study, they all show similar behavior for angular misalignment.

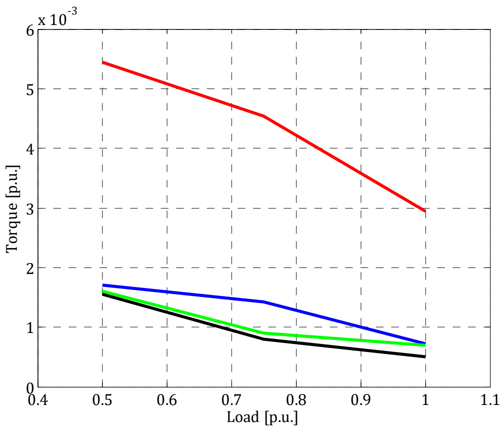

Fig. 12.26. Estimated Torque vs. percentage of load at angular misalignment of 1°. Red: Gear Coupling. Blue: Jaw Coupling. Green: Metal Ribbon Coupling. Black: Rubber Tire-type Coupling.

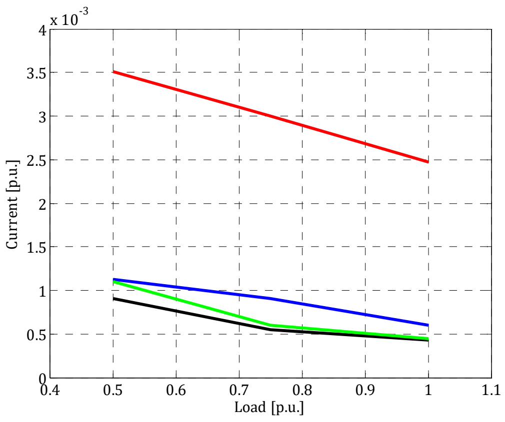

Fig. 12.27. Current components, *f*±*fr* (rms) vs. percentage of load at angular misalignment of 1°. Red: Gear Coupling. Blue: Jaw Coupling. Green: Metal Ribbon Coupling. Black: Rubber Tire-type Coupling.

Figs. 12.28 and 12.29 show results for radial misalignment. In this case, significant differences for different types of coupling are observed. The jaw coupling is the one that most clearly reflect misalignment on the fault indicators, which means low tolerance to radial misalignment. On the other hand, the Rubber Tire-type Coupling shows low fault indicators, which indicates high tolerance to radial misalignment.

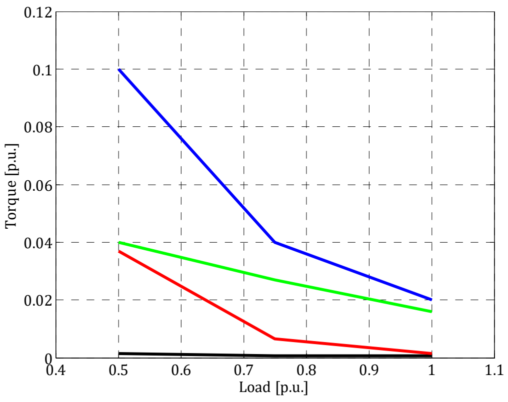

Fig. 12.28. Estimated Torque vs. percentage of load at radial misalignment of 1°. Red: Gear Coupling. Blue: Jaw Coupling. Green: Metal Ribbon Coupling. Black: Rubber Tire-type Coupling.

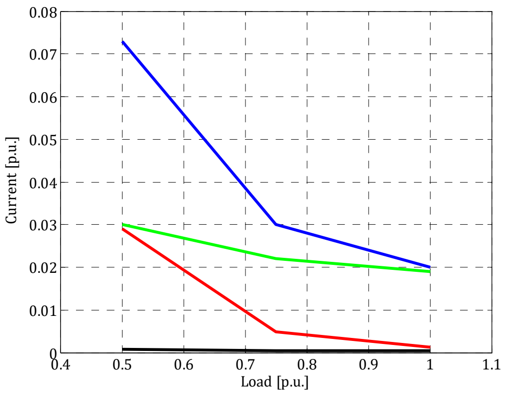

Fig. 12.29. Current components, *f*±*fr* (rms) vs. percentage of load at radial misalignment of 1°. Red: Gear Coupling. Blue: Jaw Coupling. Green: Metal Ribbon Coupling. Black: Rubber Tire-type Coupling.

From the experimental results presented in the previous section, it is concluded that both, the frequency components of the stator current (MCSA) and the estimated electrical torque (LTSA), allow identifying radial and angular misalignment when coupling induction motors and loads through flexible couplings.

Such a characteristic can be demonstrated for angular and radial misalignment and for small levels of misalignment, i.e., for incipient faults. The components of the estimated torque at $2f_r$ and $3f_r$ frequencies are suitable for detecting misalignment. The latter, however, is heavily dependent on the motor load conditions and its amplitude does not maintain, in all the cases studied, a proportional relationship with the fault levels. Therefore, it is considered a more suitable fault indicator than that of the component at $2f_r$ frequency.

Fault indicators, as for the MCSA as for the LTSA, show high dependence on the characteristic of the used coupling. This makes it difficult to associate fault indicators with a certain degree of misalignment, without considering the specific features of the coupling. Moreover, it is important to note that the coupling to more easily detect angular misalignment is the one with the lowest tolerance of angular misalignment (Gear Coupling), according to its manufacturer. Similarly, the lower radial misalignment tolerance given by the coupling manufacturer (Jaw Coupling) is more susceptible to radial misalignment detection. While it is not possible to draw definitive conclusions on this point, the relationship between the permissible misalignment of a coupling, given by its manufacturer, and the amplitude of fault indicators will be a subject of future studies.

Finally, the experimental study presented allows to state that the sensitivity of fault indicators strongly depends on the coupling features. Hence, in the case of automatic on-line fault detection algorithms, as the one proposed by [27], the thresholds above which alarm signals appear should be set depending on the type of coupling.

12.4. Gear Box Fault Detection

Faults in gear boxes can have several causes: lubrication system deficiencies, overload, fatigue, misalignment between pinion and crown wheel, and sudden blows to the gear teeth due to inconvenience in the load, among others. The consequences are the wear of gear teeth flanks, cracks in one or more teeth, fissures, teeth geometry deformation, etc. The main frequency components associated with gear failure are obtained through vibration studies. Vibrations are the result of disturbances in the torque transmitted by a gear box; therefore, the characteristic components of a fault will be reflected on the machine vibrations and on the electromagnetic torque transmitted by the motor. The main components are the rotation frequency of each gear wheel f_r, the coupling frequencies f_e, given by the result between the wheel rotation speed and the number of teeth Z ($f_e = Z f_r$), the sidebands around the gear frequencies given by ($f_e \pm f_r$), and the sidebands around the natural frequency of vibration f_{res}, or the resonance frequency of the rotating system that result in ($f_{res} \pm f_r$) [32].

This study aims to analyze the behavior of each of these frequencies in faults of variable gravity in order to identify the most appropriate failure indicators. The gear box used in the experiments has the characteristics detailed in Fig. 12.30 (a two stages reduction by means of two pinion and crown wheel sets). Table 12.6 shows the number of teeth, the module and the speed of each wheel, expressed in RPM and in revolutions per second or Hz. All the wheels have straight-teeth. The gear box is driven by an induction motor of 3 kW, 380 V, 1445 RPM. As a load it is used a DC generator which feeds a bank of resistive loads. Since the induction motor will present small variations in its speed based on the applied load, the reference speed to be considered corresponds to a load equal to 80 % of the nominal load (i.e., 1453 RPM, as seen in Table 12.6). This load state was selected with the aim of representing a very frequent situation in industrial drives.

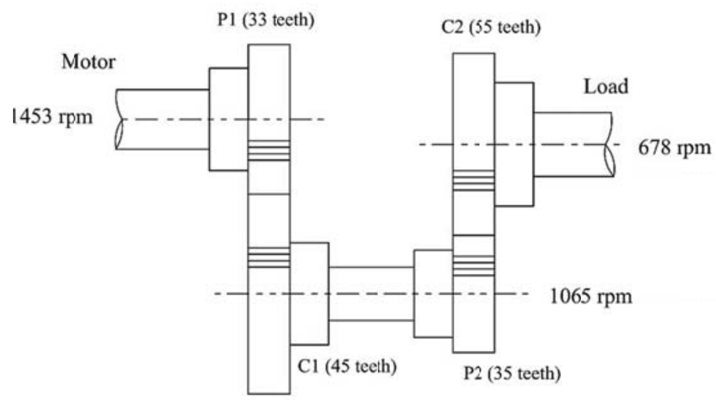

Fig. 12.30. Gear box scheme.

Table 12.6. Details of the gear box.

Gear wheel	***Z***	**Module**	***n* (rpm)**	***f* (Hz)**
Pinion 1	33	2	1453	24.21
Crown wheel 1	45	2	1065	17.75
Pinion 2	35	1,5	1065	17.75
Crown wheel 1	55	1,5	678	11.3

The gear box has three different rotation speeds, corresponding to each of its axes. The rotation frequencies, according to the right column of Table 12.6, are: f_{r1} = 24.21 Hz, f_{r2} = 17.75 Hz and fr_3 = 11.3 Hz. The gear frequencies are given by:

$$f_{e1} = Z_{P1}.f_{r1} = Z_{C1}.f_{r2} = 798.9Hz, \tag{12.16}$$

$$f_{e2} = Z_{P2}.f_{r2} = Z_{C2}.f_{r3} = 621.25Hz, \tag{12.17}$$

where Z_{P1}, Z_{C1}, Z_{P2} and Z_{C2} are the number of teeth of the pinions and crown wheel. The system resonance frequency, for its part, is given by [42]:

$$f_{res} = \frac{1}{2\pi}\sqrt{k_c \frac{J_m + J_p}{J_m J_p}}, \tag{12.18}$$

where k_c is the rotational stiffness, J_m is the motor inertia and J_p is the load inertia relative to the motor speed. For the studied case, $J_m = 0.012$ kg.m^2, $J_p = 0.037$ kg.m^2 and k_c approximately equal to 95186 Nm/rad. Therefore, the estimated resonance frequency is $f_{res} = 512$ Hz. This value is only approximate and will be corroborated or corrected considering the experimental results.

In order to test the studied fault detection technique, several gears were carved for crown wheel 2. On one of these gears, the flank of one of the teeth was rectified as shown in Fig. 12.31. The cut (dotted line) is similar to the wear that occurs on a tooth due to manufacturing or lubrication failures, among others. This fault will be hereinafter referred to as "fault 1". The other fault refers to the lack of a complete tooth. This situation, shown in Fig. 12.32, will be appointed to as "fault 2" and can be caused by tooth fatigue or due to fissures or carving faults.

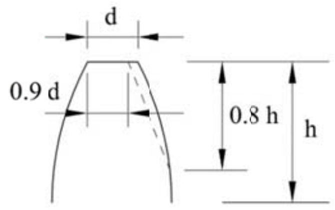

Fig. 12.31. Tooth of Crown wheel 2 with wear on the flank (fault 1).

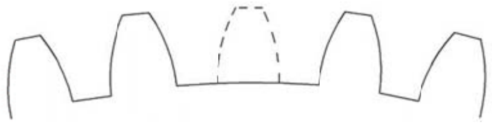

Fig. 12.32. Crown wheel 2 with missing tooth (fault 2).

The motor electromagnetic torque, according to which the diagnosis will be made, is estimated by measuring the voltages applied to the motor and the stator currents according to the model presented in [43]. The variables are acquired from a data acquisition board and are processed in MATLAB. The sampling time is 20 seconds and the sampling frequency is 10 kHz. A schematic of the set can be seen in Fig 12.33.

All the experimental tests were performed with the motor connected to the electricity network, and with a load equal to 80 % of the nominal load. First, measurements were made with the fault-free gear unit. The frequency spectrum for the estimated torque, with its components expressed in p.u., is presented in Fig. 12.34. Component at f_{r1}

corresponds to the engine speed, component at f_{r2} to the intermediate shaft and component at f_{r3} to the load. All these components are present in the toque frequency spectrum, even for the "without faults" condition, because the gear of the teeth, especially in gears of straight teeth, produces small perturbations. In addition, the geometry of the teeth may present small irregularities product of the carving process.

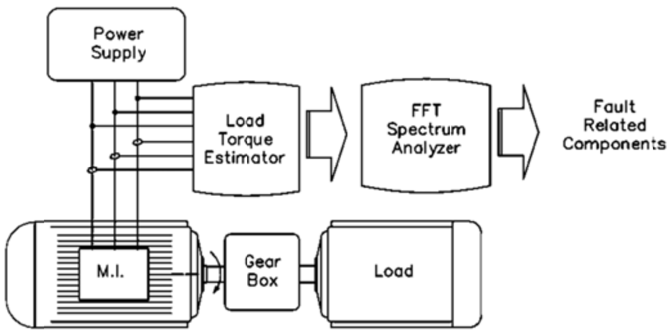

Fig. 12.33. Data acquisition and analysis system.

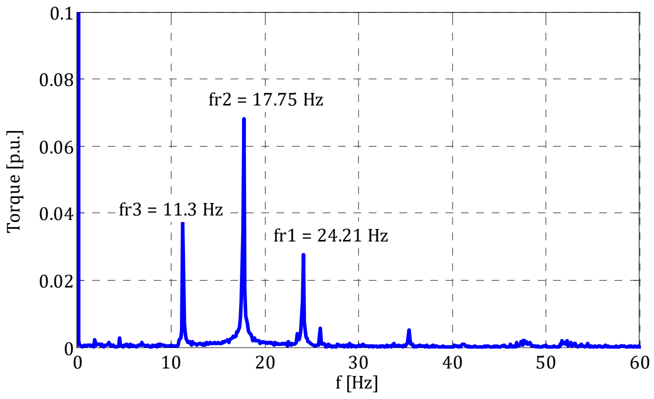

Fig. 12.34. Estimated electromagnetic torque frequency spectrum. Motor at 80 % load. Reducer without faults.

Fig. 12.35 shows the results for "fault 2" condition in gear 2. The component at f_{r3}, in this case, presents an increase of more than 100 %, whereas components at f_{r1} and f_{r2} practically maintain their value. On the other hand, the figure clearly shows harmonic components at 2 and 3 times the rotation frequency of gear 2, components that were absent in Fig. 12.34.

The gear frequency of gear 2, given by equation (12.17), is 621.25 Hz. This component is not present in the torque frequency spectrum for any of the faults tested. Fig. 12.36 shows the electromagnetic torque frequency spectrum for fault 2 condition, with the motor at

80 % of the nominal load. Fig. 12.36, therefore, shows the absence of the component at the gear frequency.

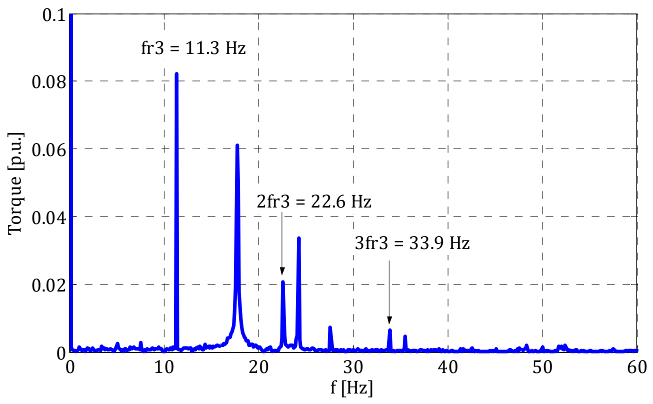

Fig. 12.35. Electromagnetic torque frequency spectrum estimated for fault 2 condition. Motor at 80 % load.

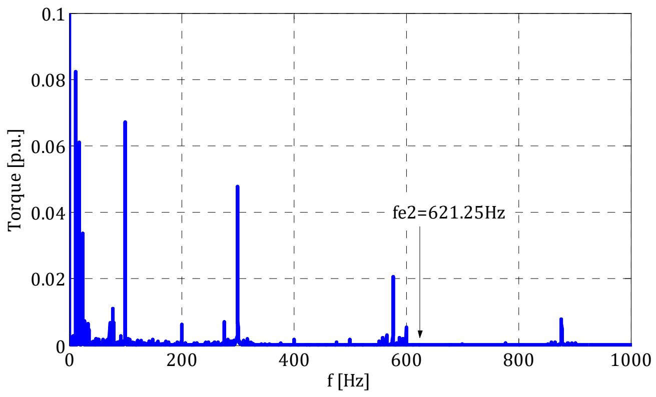

Fig. 12.36. Gear frequency proximities of crown wheel 2 for fault 2.

The resonance frequency of the system had been estimated at a value given by f_{res} = 512 Hz. Fig. 12.37 shows that in the proximity of this value, an important component is observed at 575.4 Hz. It is assumed, therefore, that the resonance frequency corresponds to that value. In addition, Fig. 12.37 shows the sidebands at $f_{res} \pm f_{r3}$. The red curve corresponds to "fault 2" and the blue to the "without faults" condition. The displacement observed between one curve and another is due to a small variation in the motor's load state and consequently in the speeds of rotation reached in each test.

The tests were repeated for the three possible fault states (without faults, fault 1 and fault 2) and for different load states. Fig. 12.38 shows the results obtained for the component at f_{r3}. Both fault states can be recognized for any motor state load. Figs. 12.39 and 12.40 show the rotation frequency multiple harmonic components, namely: $2f_{r3}$ and $3f_{r3}$. Both components have a growth proportional to the failure degree of the gearwheel and, therefore, should be considered as possible failure indicators. Finally, Fig. 12.41 shows the RMS value around the resonance frequency. This indicator, like the previous ones, allows to detect a failure situation for any of the load states tested.

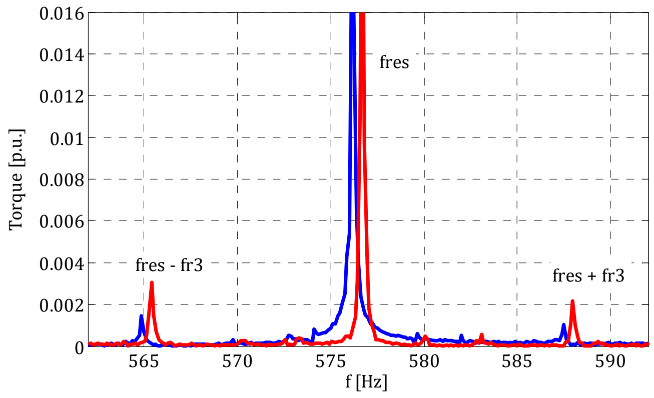

Fig. 12.37. Estimated electromagnetic torque frequency spectrum. Motor at 80 % load. Blue: without faults. Red: fault 2.

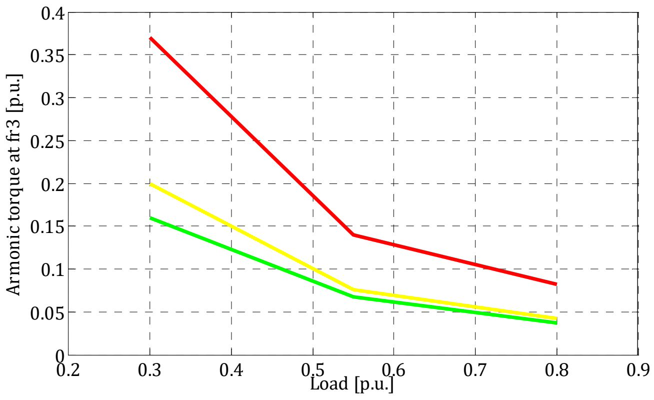

Fig. 12.38. Fault indicator (f_{r3}) depending on the load state. Green: without faults; yellow: fault 1; red: fault 2.

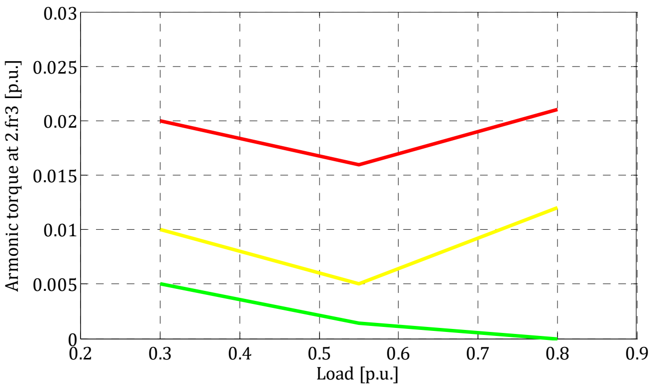

Fig. 12.39. Fault indicator ($2f_{r3}$) depending on the load state. Green: without faults; yellow: fault 1; red: fault 2.

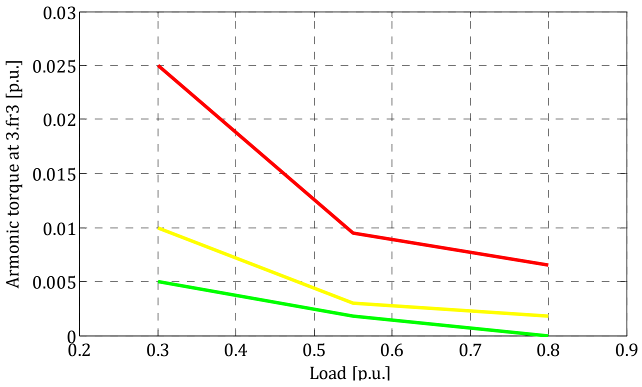

Fig. 12.40. Fault indicator ($3f_{r3}$) depending on the load state. Green: without faults; yellow: fault 1; red: fault 2.

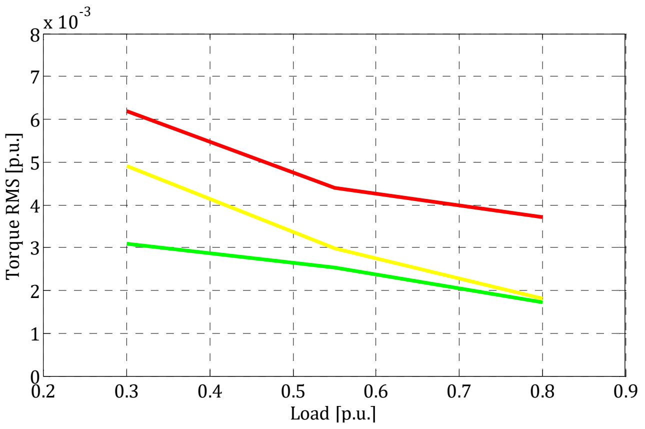

Fig. 12.41. Global fault indicator in the proximities of de f_{res} depending on the load state. Green: without faults; yellow: fault 1; red: fault 2.

Faults of different severity in a gear box were studied through the frequency analysis of the estimated electromagnetic torque. The indicator linked to the rotation frequency of the faulted wheel (f_{r3}) is the most susceptible to failure. However, its ability to identify failure situations decreases with increased motor load. The indicator at $2f_{r3}$ offers similar results but has the advantage of being less susceptible to changes in the motor load. The indicator related to $3f_{r3}$, on the other hand, follows a behavior similar to indicator f_{r3} as well as the sidebands around the resonance frequency, although in this case there is the additional difficulty of determining a priori the resonance frequency of the system. Finally, the component at the gear frequency did not show significant changes for any of the studied faults nor for any load state tested.

Since the fault indicators present significant values even without the presence of a failure, the detection method studied is only adequate when evaluating the evolution of each of the components over time. Thus, a periodic monitoring of fault indicators could lead to the detection of abnormal situations.

12.5. Conclusions

On-line fault detection techniques in electric drives have become very important in recent years. Some of them are already used at industrial level as a complement to the traditional techniques of predicvitive maintenance of electric machines.

As shown in this chapter, the ability to detect faults automatically and on-line is not limited to faults in the motor itself but can be expanded to the entire motor-driven system. Thus, electrical and mechanical faults in electrical drives can be detected and diagnosed through the techniques presented here.

As a research area, far from being exhausted, these and other diagnostic techniques continue to develop and increase its scope and reliability.

Acknowledgements

This research is supported by the Anpcyt, Conicet, Universidad Nacional Del Centro De La Provincia De Buenos Aires and Universidad Nacional De Rio Cuarto (Argentina).

References

[1]. O. V. Thorsen, M. Dalva, A survey of faults on induction motors in offshore oil industry, petrochemical industry, gas terminals, and oil refineries, *IEEE Transactions on Industry Applications*, Vol. 31, Issue 5, 1995, pp. 1186-1196.

[2]. H. Henao, G. A. Capolino, M. Fernandez-Cabanas, F. Filippetti, C. Bruzzese, E. Strangas, R. Pusca, J. Estima, M. Riera-Guasp, S. Hedayati-Kia, Trends in fault diagnosis for electrical machines: A review of diagnostic techniques, *IEEE Industrial Electronics Magazine*, Vol. 8, Issue 2, 2014, pp. 31-42.

[3]. M. Riera-Guasp, J. A. Antonino-Daviu, G. A. Capolino, Advances in electrical machine, power electronic, and drive condition monitoring and fault detection: State of the art, *IEEE Transactions on Industrial Electronics*, Vol. 62. Issue 3, 2015, pp. 1746-1759.

[4]. A. Bonnett, G. Soukup, Cause and analysis of stator and rotor failures in three-phase squirrel-cage induction motors, *IEEE Transactions on Industry Applications*, Vol. 28, Issue 4, 1992, pp. 921-937.

[5]. S. Nandi, H. Toliyat, Fault diagnosis of electrical machines – A review, in *Proceedings of the IEEE International Electric Machines and Drives Conference (IEMCD'99)*, Washington, USA, May 9-12, 1999, pp. 197-204.

[6]. C. Verucchi, C. Ruschetti, E. Giraldo, G. Bossio, J. Bossio, Efficiency optimization in small induction motors using magnetic slot wedges, *Electric Power Systems Research*, Vol. 152, Issue 11, 2017, pp. 1-8.

[7]. C. Verucchi, C. Ruschetti, F. Benger, Efficiency measurements in induction motors: Comparison of standards, *IEEE Latin America Trans*., Vol. 13, Issue 8, 2015, pp. 2602-2607.

[8]. C. Verucchi, C. Ruschetti, G. Kazlauskas, High efficiency electric motors: economic and energy advantages, *IEEE Latin America Trans*., Vol. 11, Issue 6, 2013, pp. 1326-1332.

[9]. D. F. Busse, J. M. Erdman, R. J. Kerkman, D, W. Schlegel, G. L. Skibinski, The effects of PWM voltage source inverter on the mechanical performance of rolling bearings, *IEEE Transactions on Industry Applications*, Vol. 33, Issue. 2, 1997, pp. 567-576.

[10]. M. Kaufhold, H. Auinger, M. Berth, J. Speck, M. Eberhardt, Electrical stress and failure mechanism of the winding insulation in PWM-Inverter-Fed low-voltage induction motors, *IEEE Transactions on Industrial Electronics*, Vol. 47, Issue. 2, 2000, pp. 396-402.

[11]. D. Dorrell, W. T. Thomson, S. Roach, Analysis of airgap flux, current, and vibration signals as a function of the combination of static and dynamic airgap eccentricity in 3-phase induction motors, *IEEE Trans. Ind. Applications*, Vol. 33, Issue 1, 1997, pp. 24-34.

[12]. J. R. Cameron, W. T. Thomson, A. B. Dow, Vibration and current monitoring for detecting airgap eccentricity in large induction motors, *IEE Proceedings*, Vol. 133, Issue 3, 1986, pp. 155-163.

[13]. R. Schoen, B. Lin, T. Habetler, J. Schlag, S. Farag, An unsupervised, on-line system for induction motor fault detection using stator current monitoring, *IEEE Transactions on Industry Applications*, Vol. 31, Issue 6, 1995, pp. 1280-1286.

[14]. S. Nandi, R. Bharadwaj, H. A. Toliyat, A. G. Parlos, Performance analysis of a three phase induction motor under mixed eccentricity condition, in *Proceedings of the IEEE International Conference on Power Electronic Drives and Energy Systems for Industrial Growth (PEDES'98),* Perth, Australia, Dec. 3 1998, pp. 123-128.

[15]. G. Acosta, C. Verucchi, E. Celso, A current monitoring system for diagnosing electrical failures in induction motors, *Mechanical Systems and Signal Processing*, Vol. 20, Issue 4, 2006, pp. 953-965.

[16]. C. Verucchi, G. Acosta, F. Benger, A review of fault diagnosis of induction machines, *Latin American Applied Research*, Vol. 38, Issue 2, 2008, pp. 113-121.

[17]. C. Verucchi, G. Acosta, Fault detection and diagnosis techniques in induction electrical machines, *IEEE Latin America Trans.*, Vol. 5, Issue 1, 2007, pp. 41-49.

[18]. C. Verucchi, G. Acosta, E. Caruzzo, Influencia de la inercia y el torque de carga en el diagnóstico de fallas en rotores de máquinas de inducción, *IEEE Latin America Trans.*, Vol. 3, Issue 4, 2005, pp. 48-53.

[19]. S. M. C. Cruz, A. J. M. Cardoso, Stator winding fault diagnosis in three-phase synchronous and asynchronous motors by the extended park's vector approach, in *Proceedings of the IEEE Industry Applications Conference*, Vol. 1, Roma, Italy, Oct. 2000, pp. 395-401.

[20]. H. Nejjari, M. Benbouzid, Monitoring and diagnosis of induction motors electrical faults using a current park's vector pattern learning approach, *IEEE Transaction on Industry Applications*, Vol. 36, Issue 3, 2000, pp. 730-735.

[21]. G. Salles, F. Filippetti, C. Tassoni, G. Grellet, G. Franceschini, Monitoring of induction motor load by neural network techniques, *IEEE Transactions on Power Electronics*, Vol. 15, Issue 4, 2000, pp. 762-768.

[22]. F. Filippetti, G. Franceschini, C. Tassoni, P. Vas, Recent developments of induction motor drives fault diagnosis using AI techniques, *IEEE Transactions on Industrial Electronics*, Vol. 47, Issue 5, 2000, pp. 994-1004.

[23]. P. V. Goode, M. Chow, Using a neural/fuzzy system to extract heuristic knowledge of incipient faults in induction motors, *IEEE Transactions on Industrial Electronics*, Vol. 42, Issue 2, 1995, pp. 131-146.

[24]. G. Acosta, C. Alonso, B. Pulido, Basic tasks for knowledge based supervision in process control, *Eng. App. of Artificial Intelligence*, Vol. 14, Issue 4, 2001, pp. 441-455.

[25]. C. Verucchi, J. Bossio, G. Bossio, G. Acosta, Misalignment detection in induction motors with flexible coupling by means of estimated torque analysis and MCSA, *Mechanical Systems and Signal Processing*, Vol. 80, Issue 12, 2016, pp. 570-581.

[26]. J. M. Bossio, G. Bossio, C. De Angelo, Angular misalignment in induction motors with flexible coupling, in *Proceedings of the IEEE Industrial Electronics Conference (IECON'09)*, Porto, Portugal, Nov. 2009, pp. 1033-1038.

[27]. R. Obaid, T. Hableter, Current-based algorithm for mechanical fault detection in induction motors with arbitrary load conditions, in *Proceedings of the IEEE IAS Annual Meeting,* Vol. 2, Salt Lake, USA, Oct. 2003, pp. 1347-1351.

[28]. S. Kia. H. Henao, G. A. Capolino, Torsional vibration assessment in railway traction system mechanical transmission, in *Proceedings of the IEEE International Symposium on Diagnostics for Electric Machines, Power Electronics and Drives (SDEMPED'09)*, Cargese, France, Aug. 2009, pp. 1-8.

[29]. S. Kia, H. Henao, G. A. Capolino, A comparative study of acoustic, vibration and stator current signatures for gear tooth fault diagnosis, in *Proceedings of the 20th International Conference on Electrical Machines (ICEM'12)*, 2012, Marseille, 2012, pp. 1514-1519.

[30]. S. Rajagopalan, T. G. Habetler, R. G. Harley, T. Sebastian, B. Lequense, Current/Voltage-based detection of fault in gears coupled to electric motors, *IEEE Transactions on Industry Applications*, Vol. 42, Issue 6, 2006, pp. 1412-1420.

[31]. A. Bellini, F. Filippetti, G. Franceschini, C. Tassoni, R. Passaglia, M. Saottini, M. Giovannini, Mechanical failures detection by means of induction machine current analysis: A case history, in *Proceedings of the IEEE Symposium on Diagnostics for Electric Machines, Power Electronics and Drives (SDEMPED'03)*, Atlanta, USA, Aug. 2003, pp. 322-326.

[32]. C. Verucchi, G. Bossio, J. Bossio, G. Acosta, Fault detection in gear box with induction motors: an experimental study, *IEEE Latin America Trans.,* Vol. 14, Issue 6, 2016, pp. 2726-2731.

[33]. M. Stopa, J. Braz, J. Cardoso Filho, C. Martinez, Incipient detection of cavitation phenomenon in centrifugal pumps, *IEEE Transactions on Industry Applications*, Vol. 50, Issue 1, 2014, pp. 120-126.

[34]. P. C. Krause, Analysis of Electric Machinery, *McGraw-Hill Book Company*, 1986, pp. 164-210.

[35]. W. T. Thomson, M. Fenger, Current signature analysis to detect induction motor faults, *IEEE Industry Applications Magazine*, Vol. 7, Issue 4, 2001, pp. 26-34.

[36]. S. M. A. Cruz, A. J. M. Cardoso, Diagnóstico de avarias no rotor de motores de indução trifásicos, in *Proceedings of the 5º Congesso Nacional de Manutenção Industrial*, Figueira da Foz, Portugal, Oct. 23, 1996, pp. 1-8.

[37]. R. Schoen, T. Habetler, Effects of time-varying loads on rotor fault detection in induction machines, *IEEE Transactions on Industry Applications*, Vol. 31, Issue 4, 1995, pp. 900-906.

[38]. R. Obaid, T. Hableter, Effect of load on detecting mechanical faults in small induction motors, in *Proceedings of the Symposium on Diagnostics for Electric Machines, Power Electronics and Drives (SDEMPED'03)*, Atlanta, USA, Aug. 2003, pp. 307-311.

[39]. J. Piotrowski, Shaft Alignment Handbook, 3rd Ed., *CRC Press*, Ohío, 2006.

[40]. M. Stopa, B. de Jesus Cardoso Filho, Load Torque Signature Analysis: An alternative to MCSA to detect faults in motor driven loads, in *Proceedings of the IEEE Energy Conversion Congress and Exposition (ECCE'12)*, Raleigh, USA, 2012, pp. 4029-4036.

[41]. C. Salomón, W. Santana, L. da Silva, E. Bonaldi, L. de Oliveira, J. da Silva, G. Lambert-Torres, A. Donadon, A stator flux synthesis approach for torque estimation of induction motors using a modified stator resistance considering the losses effect, in *Proceedings of the IEEE International Electric Machines & Drives Conference (IEMDC'13)*, Chicago, USA, May. 2013, pp. 1369-1375.

[42]. S. Kia, H. Henao, G. Capolino, Gear tooth surface damage fault detection using induction machine stator current space vector analysis, *IEEE Transactions on Industrial Electronics*, Vol. 62, Issue 3, 2015, pp. 1866-1878.

[43]. T. Sutikno, A. Jidin, A. Idris, FPGA based high performance torque and flux estimator, *International Review of Electrical Engineering*, Vol. 6, Issue 1, 2013, pp. 207-214.

Index